


Article

The Formation and Disintegration of Rafts from Different Aluminas and Fines

Sindre Engzelius Gylver ^{1,*}, Simen Bekkevoll ¹, Stein Rørvik ² and Kristian Etienne Einarsrud ¹ 

¹ Department of Materials Science and Engineering, Norwegian University of Science and Technology NTNU, NO-7491 Trondheim, Norway

² SINTEF Industry, Metal Production and Processing, NO-7465 Trondheim, Norway

* Correspondence: sindre.e.gylver@ntnu.no; Tel.: +47-48252061

Abstract: Raft formation is a frequently encountered problem during alumina feeding in the Hall-Héroult-process and will delay alumina from being dissolved into the melt. The mechanisms for the formation and disintegration of rafts are however not thoroughly understood yet. The current study investigates the dissolution behavior and raft structure from three different types of secondary alumina in a lab cell, with a particular attention to effect of fines, and involves both sampling of rafts and video recordings of the feeding. The mass loss rate was calculated to vary between -1.57 and -0.42 g min⁻¹ for regular bulk alumina, and -1.15 and -0.06 g min⁻¹ for fines. Rafts created from bulk alumina were flat with a distinct bulge or crater placed in the center of it, while rafts created from fines had a pellet-shaped structure and traces of undissolved alumina in the middle. The observed structure is due to the initial spreading of powder, confirmed by video recordings.

Keywords: aluminum production; alumina feeding; raft; fines



Citation: Gylver, S.E.; Bekkevoll, S.; Rørvik, S.; Einarsrud, K.E. The Formation and Disintegration of Rafts from Different Aluminas and Fines. *Metals* **2022**, *12*, 1876. <https://doi.org/10.3390/met12111876>

Academic Editor: Mark E. Schlesinger

Received: 27 September 2022

Accepted: 27 October 2022

Published: 3 November 2022

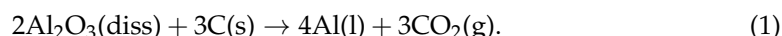
Publisher's Note: MDPI stays neutral with regard to jurisdictional claims in published maps and institutional affiliations.



Copyright: © 2022 by the authors. Licensee MDPI, Basel, Switzerland. This article is an open access article distributed under the terms and conditions of the Creative Commons Attribution (CC BY) license (<https://creativecommons.org/licenses/by/4.0/>).

1. Introduction

Aluminum is today produced by the Hall-Héroult-Process, where alumina is dissolved into a cryolitic melt and aluminum is formed by an electrochemical reaction together with carbon:



The process is carried out at approximately 960 °C, and alumina is added regularly from point feeders, placed at one or several position in the cell. Ensuring an efficient dissolution and distribution of alumina is important in order to maintain stable operations. When added to the melt, some particles might agglomerate together and create rafts, consisting of alumina and frozen bath. These rafts hinders contact between powder and liquid, and must hence disintegrate and the frozen bath must melt in order for alumina to be further dissolved [1].

Studies of rafts have been intensified over the last years, and formation of rafts has been recorded in industrial cells [2], where bath circulations and temperature were found to affect the raft floating time, together with the moisture and fluoride content of the alumina. By extracting samples from the cell and further processing them by micro X-ray computed tomography (μCT), it is revealed that the rafts are porous structures with an average density of 1.76 g/cm³ and a porosity of 12.72% [3]. Earlier results by Walker et al. [4] found the apparent density of collected agglomerates to be between 2.2 and 2.4 g/cm³ and porosities between 24.7 and 22.8% in the time span of 15–60 s. However, both the sampling technique and characterization method is different, which might be the cause of the varying results.

The effect of different parameters has mainly been studied at lab scale, where one of the largest studies has been conducted by Kuschel and Welch [5,6]. They observe that the cell conditions, in particular electrolyte velocity and superheat, can affect the

dissolution time with 300–500%. The alumina properties can affect the dissolution time by approximately 50%, and properties summarized to promote fast dissolution were a high volatile content, i.e., high loss on ignition (LOI), and low flow funnel time, where the latter one is closely related to particle size distribution (PSD). It is in accordance with findings by other researches [7,8]. Fines have been reported to be problematic in operations [9], as they are harder to transport and feed to the cells, and poorer wetting will inhibit dissolution.

Bath properties will also affect the dissolution rate, and recently, Alarie et al. [10] developed an empirical equation based on results from their own [11] and several other research groups [7,12–14], where only the bath temperature, AlF_3 - and Al_2O_3 -content were found to be significant, and is used as input parameters.

Retrieving samples from a lab-cell has been conducted in earlier work, where rafts with a similar structure as industrial one were collected, and the effects of alumina temperature [15], adsorbed water content and dry-scrubbing have been studied [16]. From the latter one it was observed that rafts created from secondary alumina had a higher porosity than those formed from primary. This is in accordance with studies on alumina crusts [17], where a lower density and hence higher porosity were found, and it was concluded that carbon content in the powder was the origin of the pores. Kaszás [18] did however find that rafts from alumina with a higher content of moisture were more porous.

Equipment suitable for observing the alumina addition has also become more common in recent years. The development of see-through cells, containing a quartz crucible which becomes transparent when heated up, and enables the opportunity for observing dissolution from the side. When secondary alumina is added, the powder stays on the interface before particles and fragments sink into the bath and are gradually dissolved [19,20]. It is believed that the effect of volatiles, in particular carbon dust, is emphasized as an important parameter for faster dissolution in these setup [21].

Kaszás et al. [22] recorded the spreading and disintegration from above in a 7.6 cm × 7.6 cm squared crucible, and provided image analysis to measure the visible surface area, which was found to be between 25 and 20 cm² 5 s after addition. A rapid decrease in surface area was observed for the first 25 s after feeding, before stabilizing with a more or less constant surface area. For the addition of 1 g alumina, the powder gets fully wetted within the first 10 s after addition, and rafts stay afloat on the surface for a long period, up to 5 min for 1 g additions and 10 min for addition of 2 g. Later, the effect of adding carbon to alumina was studied [18]. A challenge for this setup is to preserve heat, and the top was therefore covered with a plate of quartz during parts of the experiments.

The current work studies the dissolution and the structure of rafts formed from different types of secondary alumina and their corresponding fraction of fines. Experiments with these types have already been carried out in a see through-cell [20,23], hence gaining a foundation for comparison of different setups.

2. Methods and Materials

2.1. Materials

For each alumina used in the current work, two batches denoted as bulk and fines will be considered. The bulk alumina represents the alumina used in the industry, with a typical PSD between 0 and 250 µm. Alumina fines consist of sieved out alumina grains with a particle size ≤ 45 µm. The PSD is obtained by laser diffraction with the results displayed in Figure 1, analyzed by Hydro Aluminium.

Physicochemical properties are given in Table 1, while the content of impurity elements are shown in Table 2. Moisture on ignition (MOI) and LOI were measured using the ISO-standard, while the other properties were determined by Hydro Aluminium, using industry standard measurements.

The industrial bath was also analyzed by Hydro Aluminium, where the most essential features of the bath are listed in Table 3 with liquidus and solubility limit estimated from empirical Equations [24,25].

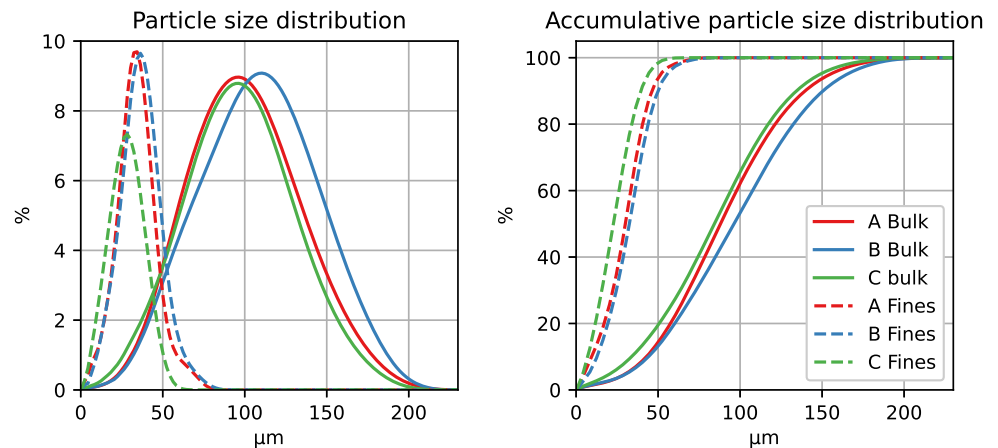


Figure 1. PSD of the different aluminas displayed to the left, and accumulative PSD to the right.

Table 1. Selected alumina properties.

Alumina Type	LOI (1000 °C) [%]	MOI (300 °C) [%]	BET Surface [m ² /g]	α Alumina [%]	γ Alumina [%]
A bulk	1.86	1.5	73.9	1.2	39.7
B bulk	2.11	2.65	65	2.5	37.2
C bulk	2.33	1.7	69.8	1.8	38.1
A fines	4.54	1.84	55.2	4.5	35
B fines	5.59	2.33	43.8	9.3	30.4
C fines	5.03	1.36	52.4	7.4	32

Table 2. The content in wt% of the different elements found in alumina samples.

Alumina	F	C	S	Na	P	Ca	Fe
A bulk	1.2	0.22	0.32	0.5634	0.0017	0.0129	0.0127
B bulk	1.75	0.24	0.24	0.5389	0.0021	0.018	0.0194
C bulk	1.96	0.26	0.21	0.5089	0.0023	0.0086	0.0123
A fines	4.69	1.74	0.23	1.6868	0.0174	0.1105	0.1065
B fines	5.21	2.52	0.23	1.6568	0.0125	0.0883	0.0845
C fines	4.55	2.04	0.26	1.367	0.0107	0.0548	0.0661

Table 3. Chemistry and calculated properties of the industrial bath at initial concentrations.

Bath Chemistry	
Bath acidity [wt%]	10.6
CaF ₂ [wt%]	5.34
Al ₂ O ₃ [wt%]	3.82
Bath Properties	
Superheat	13.5
Liquidus temperature [°C] [24]	956.5
Bath temperature [°C]	970
Al ₂ O ₃ solubility limit [wt%] [25]	8.62

2.2. Setup

Both raft sampling experiments and video recordings were conducted in the same customized tube furnace with an open top, sketched in Figure 2a). The furnace body consists of a steel pipe with an inner diameter of 15 cm and is heated with an element wound around its body. The outer shell of the furnace is coupled to a water-cooled system and thermal insulation is put on the top to preserve heat as long as practical possible. A carbon crucible with an inner diameter of 10.5 cm is placed inside the furnace body, filled with 1500 g of industrial bath. Nitrogen gas is purged into the furnace environment to avoid oxidation and air burn of the carbon crucible. A thermocouple (S-type) is placed inside a steel tube to monitor the bath temperature regularly, approximately 4 cm below the bath surface. Alumina is fed through a 50 cm long steel pipe with an inner diameter of 1 cm with a spring-driven lid at the end, operated by a knob at the top. The dose is released 5 cm above the bath surface, and one dose of 4 g alumina is fed each time, both for raft sampling experiments and video recordings. Following the extraction of a raft, the bath surface was cleared mechanically and the system was allowed to reach the sought operating temperature before a new batch was fed. Typically, the time interval between the feedings was 30–45 min.

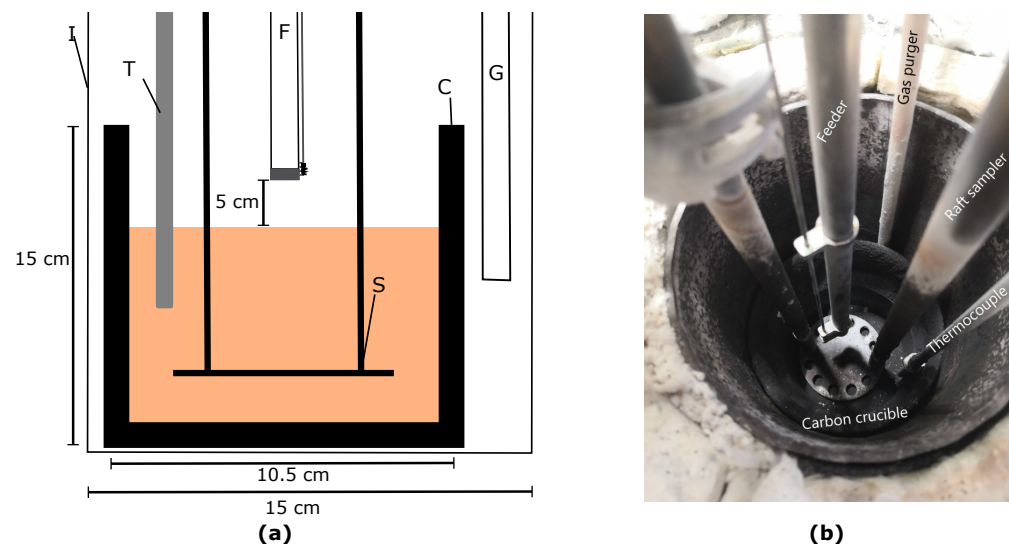


Figure 2. (a) Cross sectional illustration of the furnace. I represents the furnace body with its inner diameter, C is the carbon crucible with dimensions, G is the pipe used for gas purging, and S is the sampler used for raft sampling. T is the tube holding the thermocouple, and F is the feeder. (b) The experimental setup in cold conditions with all the equipment used.

A custom designed raft sampler is used to collect the rafts formed on the bath surface and is immersed into the melt prior to alumina feeding. It is made of stainless steel and consists of an 8 cm diameter plate, with ten holes of 1 cm diameter drilled around its periphery. Two solid steel rods are welded onto the steel plate to work as handlebars when the sampler is lowered and raised in the melt. An image of the experimental setup for raft sampling is shown in Figure 2b). Rafts are retrieved from the melt after 60 and 180 s, and a minimum of 5 rafts from each time interval were sampled.

Selected raft samples were analyzed using micro-computed X-ray tomography (μ CT). The μ CT data was acquired by a Nikon C1 compact large-envelope 5-axis X-ray μ CT instrument (cone beam volume CT). A tungsten 225 kV UltraFocus reflection target was used, with an acceleration voltage of 125 kV and a current of 175 μ A. The X-rays were not filtered. The imaging was done with an integration time of 250 ms, amplification of 18 dB, with 6283 projections per 360°. The detector panel in the instrument is a Varex 1621 EHS with 2000 \times 2000 pixels of size 200 \times 200 μ m, total panel size 40 \times 40 cm². The distance from source to sample was 174.06 mm, distance from source to detector was 772.78 mm,

resulting in a voxel size of 90.1 μm . The images were exported as 16-bit TIFF and processed in the public domain software ImageJ [26] using scripts developed at SINTEF.

Minor changes in the experimental setup are done to facilitate video recording of the dissolution process. A GoPro Hero8 Black camera is used to record the surface, and is placed inside a transparent camera house mounted to a flexible arm attached to the frame holding the furnace set-up. To limit the disturbance of fume during recording and ensure some cooling of the camera house, a fan was placed under the flexible arm holding the camera, as seen in Figure 3. The recording and the sampling experiments were conducted separately from each other, as the sampler would hinder the view for the camera.

Lastly, experiments at room temperature were conducted, where alumina was released from 5 cm onto a flat surface with the same feeding pipe as described earlier.



Figure 3. Image of the experimental setup with the camera placed above the surface opening.

3. Results

The mass gain, interpreted as the mass of the raft subtracted from the total dose added, is plotted in Figure 4, including a 95% confidence interval. The mass loss rate for the types with its 95% confidence interval is given in Table 4.

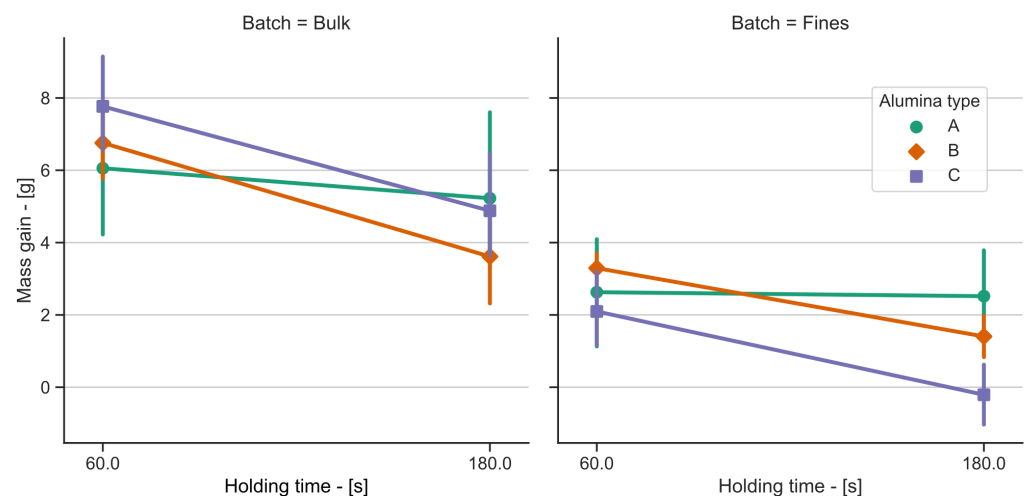


Figure 4. Mean mass gain of rafts, given as the difference between raft weight and mass alumina added, for bulk (left) and fines (right) of the three alumina types A, B and C. The error bars indicate the 95% confidence interval.

Table 4. Mass loss rates and 95% Confidence interval for the different alumina types.

Batch	Type	Mass Loss Rate [g/min]	95% Confidence Interval
Bulk	A	−0.42	[−2.04, 1.21]
	B	−1.57	[−2.64, −0.50]
	C	−1.44	[−2.61, −0.28]
Fines	A	−0.06	[−1.32, 1.21]
	B	−0.94	[−1.41, −0.48]
	C	−1.15	[−2.04, −0.27]

Figure 5 states the correlation coefficients between the mass gain at 60 s holding time and selected parameters. Correlation between other parameters are also shown in the same figures.

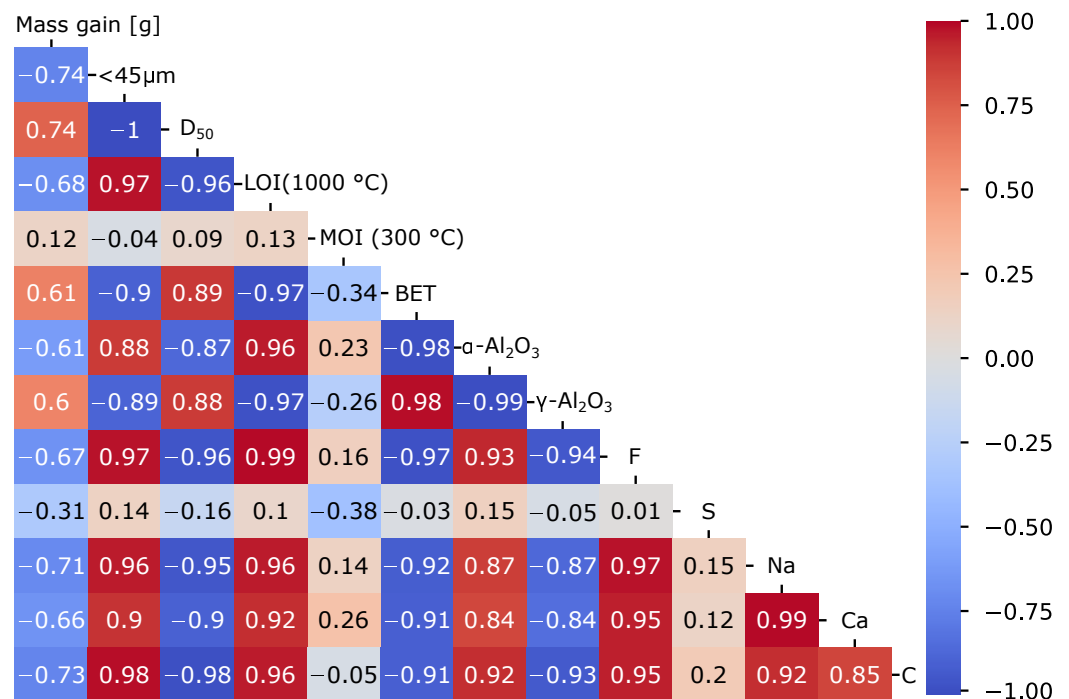


Figure 5. Correlation coefficients between selected parameters and the mass gains of samples after holding time 60 s. <math><45\mu\text{m}</math> is fraction of grains below 45 μm , while D_{50} corresponds to the width of the particle size distribution curve shown in Figure 1.

Three cross-sectional CT-images are shown in Figure 6 for two rafts from bulk alumina after 60 and 180 s and one raft created from fines. The grey values are proportional to the X-ray linear attenuation at the given volume point. The linear attenuation coefficient depends on both the density and the atomic weight of the material; where the atomic weight has a higher influence than the density. Average apparent porosity measurements between bulk, fines and holding time are displayed in Figure 7, reported as a percentage of pores relative to the entire volume of the sample (including the pores). Density is calculated as the measured mass of raft divided by the volume obtained from CT-analysis, and was on average 2.25 g cm^{-3} for bulk and 2.18 g cm^{-3} for fines. No significant difference between the different types was seen, and it was therefore chosen to only compare bulk and fines in general.

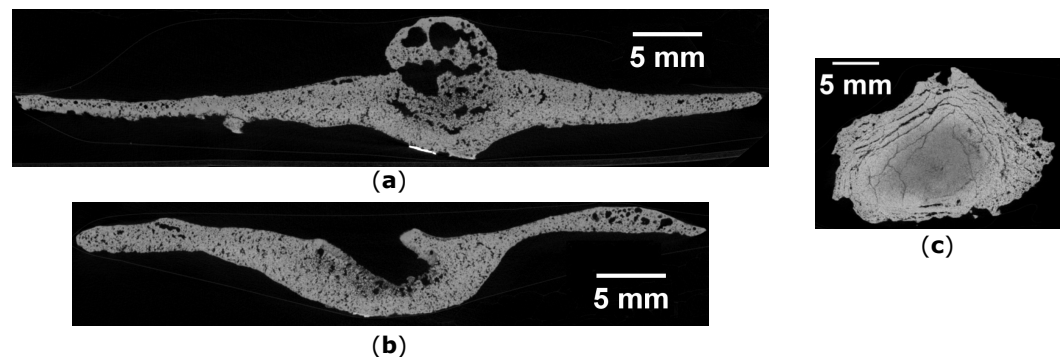


Figure 6. Cross-sectional CT images of selected rafts, where the raft's top is facing upwards. (a) Raft from bulk alumina with holding time 60 s. (b) Raft from bulk alumina with holding time 180 s. (c) Raft from fine alumina with holding time 60 s.

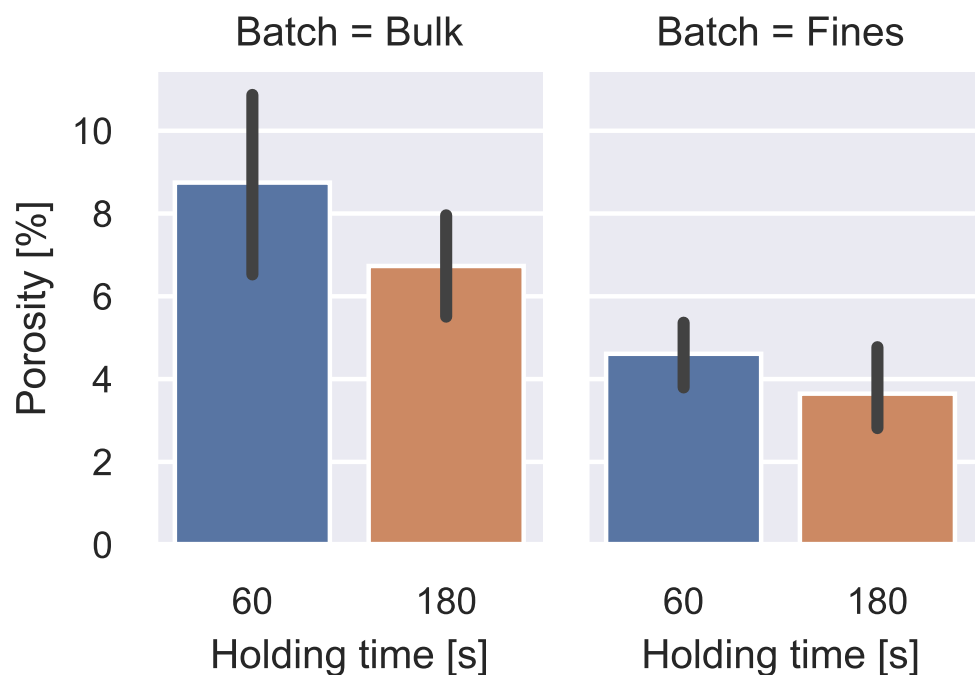


Figure 7. Mean porosity for the bulk and fine samples for the different holding times, reported as a percentage of pores relative to the entire horizontal cross-sectional area of the sample (including the pores).

CT images provided the opportunity to generate 3D plots of the rafts, using the “Interactive 3D Surface Plot” plugin in ImageJ. The 3D plots are generated from projection images, representing the average attenuation values in the Z-direction, shown in Figure 8d). By processing the images further, values corresponding to density and thickness of the rafts can be obtained, showed, respectively, for (b) and (c) in Figures 8 and 9.

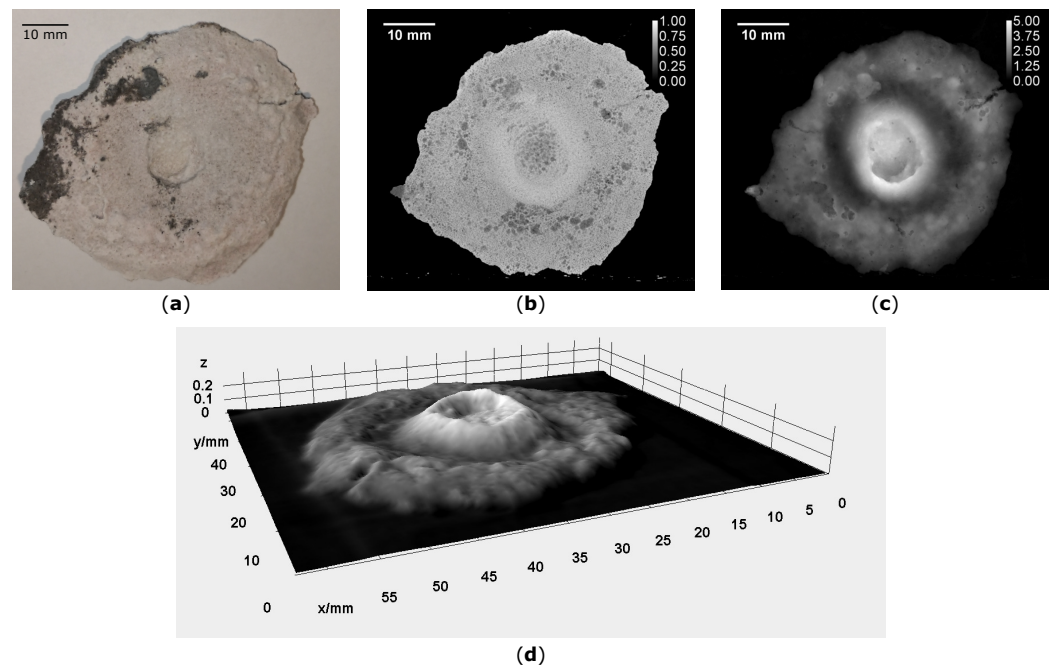


Figure 8. Images of a raft from alumina bulk type B. (a) Image of raft from above. (b) Projected CT image of the raft seen from above, displaying the average density. (c) Projected CT image of the raft seen from above, displaying the thickness of the raft. The scale is given in mm. (d) 3D-image plot seen from the side.

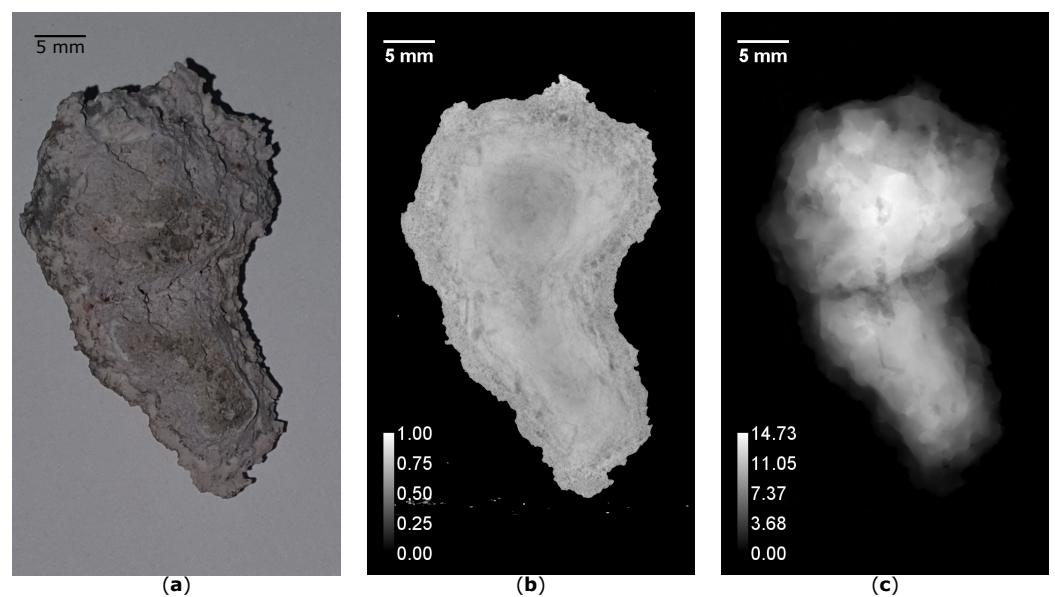


Figure 9. Images of a raft from alumina fines type A. (a) Image of raft from above. (b) Projected CT image of the raft seen from above, displaying the average density. (c) Projected CT image of the raft seen from above, displaying the thickness of the raft. The scale is given in mm.

One video recording of each of the alumina types from the bulk and fines batch was performed during the experimental session. The videos were later treated in ImageJ [26] to measure raft area as a function of time. As the quality of the recordings was not adequate for a fully automated image analysis, raft area was measured by using a brushing tool in ImageJ on the slides with sufficient quality. The measurements performed in ImageJ are displayed in Figure 10, where the time axis is logarithmic to visualize initial dispersion better. The sinking of small subrafts denoted as a, b and c, are shown in detail in Figure 11. Selected images of the initial raft formation from fines are shown in Figure 12.

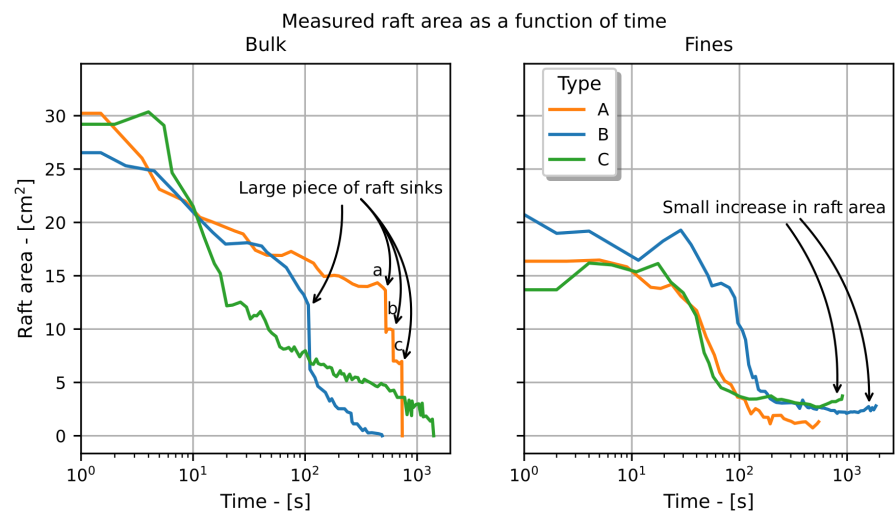


Figure 10. Measured raft area as a function of time, where a, b and c denotes sinking of rafts pieces, which can be seen more detailed in Figure 11.

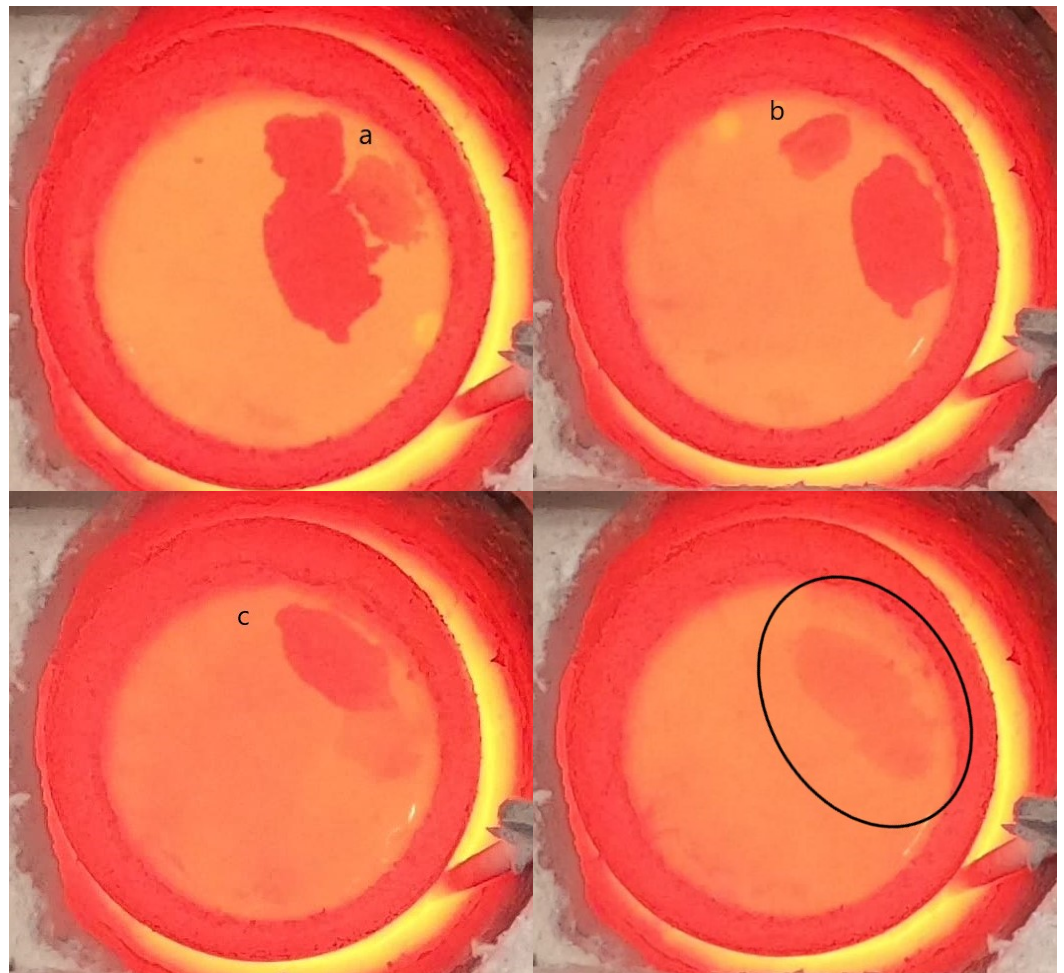


Figure 11. Images of descending subrafts (a–c) of bulk alumina type A, denoted in Figure 10. In the last frame, it is possible to see the descended rafts on the bottom of the crucible.

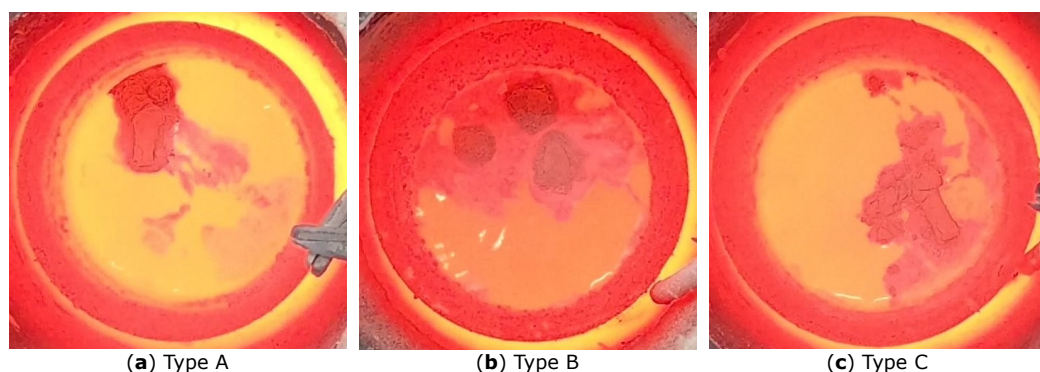


Figure 12. Selected images from the video recording of fines, selected from right after feeding to display the dispersion.

Initial dissolution rate in Table 5 is calculated as the rate the surface is disintegrated in $\text{cm}^2 \text{s}^{-1}$ at steepest part of the curve in Figure 10, normalized with the initial surface area.

Table 5. Initial rate of surface dissolving in $\text{cm}^2 \text{s}^{-1}$ at steepest part, set relative to the measured area of raft at $t = 0 \text{ s}$.

Type	Batch	Initial Dissolution Rate [%/s]
A	Bulk	−0.38
	Fines	−0.08
B	Bulk	−0.54
	Fines	−0.13
C	Bulk	−0.57
	Fines	−0.09

When a dose was fed on a flat plate, it spreads out as a circular structure, shown in Figure 13. A similar structure was seen for fines, although it spread out more poorly and created a higher heap.

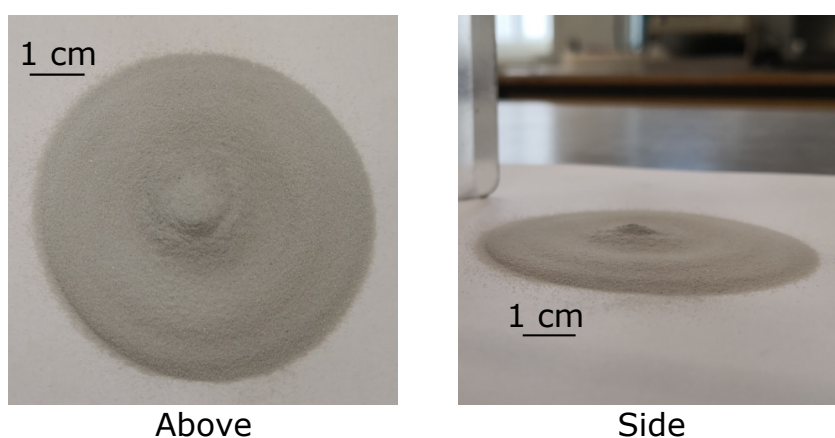


Figure 13. Results of cold experiments for bulk alumina, type A.

4. Discussion

There are characteristic differences between the rafts collected from bulk and fines. Rafts created from the bulk have more than doubled in size relative to the amount added (4 g), where the increased mass must be due to bath freezing around the cold particles, while the mass gain for fines are significantly lower, in particular after 60 s. Rafts created from fines are shaped as compact pellets, being smaller in size and mass, seen in Figure 9a).

Bulk alumina disperse well on the bath surface to form larger disc-shaped rafts of frozen bath and alumina, floating on the bath surface with a distinctive bulge or crater at the center, as seen in on the CT-images of bulk alumina in Figure 6. The darker gray scale at the center of the raft from fines shown in the same figure indicates unsaturated alumina at the core encapsulated with frozen bath around it. The video recordings support this where the powder stays together in one or a few lumps.

The dissolution behavior of different types investigated seems to vary. As seen in Table 4, alumina type B and C have calculated mass rates which are significant below zero, while this is not the case for type A. A similar tendency is seen for the corresponding fines for the different types as well, and the initial dissolution rate from the video recordings (Table 5) also indicates that A disintegrate slower at the beginning.

The correlation matrix in Figure 5 shows that the increased fraction of fines decreases the mass of formed rafts at a holding time of 60 s, with a similar trend seen at 180 s. In this setup, fines generate smaller rafts, but in general, fines have a negative impact on the dissolution, also seen by the lower rates in Table 4. Figure 5 also reveal that fines are closely related with several of the other parameters and it is therefore not possible to conclude if any other of the parameters affect the mass of the formed raft.

The errorbars in Figure 4 and confidence intervals in Table 4 reveal that there still is variation present in the dataset. As commented by Kuschel and Welch [5] operating conditions, in particular superheat and convection will affect the dissolution rate in a larger degree than alumina properties. In the current setup, it was not possible to monitor the temperature or observe the bath surface during the sampling experiments. As such, the observed variation may be due to these factors.

Earlier work in same setup [15] calculated a dissolution rate of 0.8 g/min, which is in the same order as the current experiments. Since the lab conditions are within the validity range of the model by Alarie et al. [10], predicted dissolution rate can be calculated and compared with the observed one. Assuming the $m_{ref} = 2.4689$, the predicted dissolution rate will be 0.63 g min^{-1} for all the types, as the empirical equation only uses bath properties as variables. Four out of six of the rates are found to be above predicted one, which should be expected, as the rate calculated in these set of experiments are not the actual dissolution rate of alumina, but rather the mass loss rate of rafts, which will include melting of bath. Therefore, the current dissolution measurements, at least for type B and C are within an expected range.

Common for all rafts from the bulk is the porous structure with irregularities in pore size and shape as seen in Figure 6. Larger cavities are mostly observed at the centre bulge, with some randomly scattered pores varying in size in the periphery. Additionally, all rafts from the bulk have a similar grayscale throughout the sample, indicating that the sample has a relatively homogeneous composition of bath and alumina. The calculated porosity shown in Figure 7 is higher for rafts from bulk aluminas after 60 s. A probable cause for the behavior can be seen in Figure 6, where a large pore is located inside spherical lump, which is melted away after 180 s for most samples. Earlier results in the same setup [15,16] have found porosity values around 8%, which is similar with the findings in this work.

The 3D-images give valuable information of the raft structure. For the bulk alumina, the darker areas in (Figure 8b) shows pores, which is scattered around the rafts. In addition (Figure 8c) shows that the rafts is at its thickest at in the middle. Disintegration will therefore begin from the sides, since it is the most porous and thinnest areas. Rafts from fines (Figure 9) are thicker and fewer pores, and will hence disintegrate more slowly. Another interesting finding is the similarities between the rafts (Figure 9) and the cold experiments shown in Figure 13. This indicates that the addition method is the dominating factor for the raft shape, not solidification of bath.

Video recordings provide valuable observations of the raft formation and alumina dissolution. As seen from the recordings and the images, well-dispersed alumina dissolves immediately or relatively fast within the first 30–60 s, while agglomerate forms to stay afloat on the bath surface. Raft A (Figure 11) is disintegrated into smaller parts that sink to

the bottom of the crucible, while a large piece sinks for type B, seen in Figure 10. This in accordance with observations from the see through cell [19,20]. Similar tendencies are also seen when recording from above [22] with a faster dissolution the first 25 s after addition, and sinking of rafts at the end.

The small pellets from the fines managed to stay afloat until the camera shut down due to overheating. No distinct difference in dissolution rate and behavior could be seen from the curves in the graph from Figure 10. The end of the curves shows a small increase in surface area for types B and C, due to a lack of heat at the bath surface. Insufficient heat causes more bath to freeze onto the floating raft, preventing it from sinking into the melt as it becomes more hydrostatically stable, an issue also faced by Kaszás et al. [22]. The dissolution might also be delayed as the bath close to the raft gets saturated with alumina and will not be transported away from the raft, due to small degree of convection present.

Considering the findings of Bracamonte [23], who studied the same alumina types in their dissertation, observations of the dissolution process are very similar to the ones obtained in this work. For the bulk alumina, type A had the best dispersion on the bath surface as it tended to form rafts with a large surface area, but dissolved slower. Alumina B and C dissolved faster, and no significant difference is found between them. The fine alumina showed less dispersion after feeding and was found to have a more compact crust characterized by a finer porosity, i.e., smaller pores, which is also observed in the CT images. The main deviation are trends in dissolution behavior across batches for alumina type A, where Bracamonte did not notice any significant difference between the bulk and fines for alumina type A during their experiments, contrary to the result in the current experiments. In this setup, the added amount of alumina relative to the bath volume is much lower creating one or several floating rafts, while in the see-through cell a crust like structure was created on the top.

5. Conclusions and Further Work

The current work has investigated the raft formation of different alumina types, with a special attention of rafts formed from the fine particles in a batch. In this setup, the types exhibited different behavior for raft formation. Type A had the best initial dispersion, but its mass loss rate was slower. It is however not possible to conclude why type A is behaving different. The surface properties of the particles is not investigated in this work, and will be considered in further work.

Rafts formed from fines were initially smaller than those formed from bulk, with an average mass loss rate of -0.71 vs. -1.15 g min⁻¹. CT revealed that the rafts from fines are more inhomogeneous, with powder encapsulated within a layer of frozen bath. The reduced spreading of powder results in lesser freeze of bath, and thus a reduced mass gain. The fraction of fines were in this work found to be correlated with multiple of the other properties investigated, and it is thus not possible to identify if there are any other parameters that affect the mass gain of rafts.

Recordings from above reveal that the shape of the raft is mainly dependent on how the powder spread out when added, and comparison with cold experiments supported it. Solidification of bath and agglomeration then strengthen the structure and disintegration will further occur from the sides.

In a real cell, convection is created by gas bubbles generated under the anodes and movement in the metal pad caused by magnetic fields, and is found to affect the dissolution in a larger degree [5] than alumina properties. This might be the case for the disintegration and dissolution for rafts as well. Performing further experiments with stirring should therefore be considered, although it might requires a change in sampling technique.

Author Contributions: Conceptualization, S.E.G. and K.E.E.; Data curation, S.E.G. and S.B.; Formal analysis, S.B. and S.R.; Investigation, S.E.G., S.B., S.R. and K.E.E.; Methodology, S.E.G., S.B. and S.R.; Supervision, K.E.E.; Writing—original draft, S.E.G.; Writing—review & editing, S.B., S.R. and K.E.E. All authors have read and agreed to the published version of the manuscript.

Funding: This work has been funded by the SFI Metal Production, (Centre for Research-based Innovation, 237738). The authors gratefully acknowledge the financial support from the Research Council of Norway and the partners of the SFI Metal Production.

Data Availability Statement: The data presented in this study are available on request from the corresponding author.

Acknowledgments: The authors would also like to acknowledge the use of the Pore Imaging Laboratory (NO3.7d) at SINTEF Industry, Research infrastructure under ECCSEL-ERIC.

Conflicts of Interest: The authors declare that they have no conflict of interest.

References

1. Lavoie, P.; Taylor, M.P.; Metson, J.B. A Review of Alumina Feeding and Dissolution Factors in Aluminum Reduction Cells. *Metall. Mater. Trans.* **2016**, *47*, 2690–2696. [[CrossRef](#)]
2. Gylver, S.E.; Omdahl, N.H.; Prytz, A.K.; Meyer, A.J.; Lossius, L.P.; Einarsrud, K.E. Alumina Feeding and Raft Formation: Raft Collection and Process Parameters. In *Light Metals 2019; The Minerals, Metals & Materials Series*; Chesonis, C., Ed.; Springer: Cham, Switzerland, 2019; pp. 659–666. [[CrossRef](#)]
3. Gylver, S.E.; Omdahl, N.H.; Rørvik, S.; Hansen, I.; Nautnes, A.; Neverdal, S.N.; Einarsrud, K.E. The Micro- and Macrostructure of Alumina Rafts. In *Light Metals 2019; The Minerals, Metals & Materials Series*; Chesonis, C., Ed.; Springer: Cham, Switzerland, 2019; pp. 689–696. [[CrossRef](#)]
4. Walker, D.I.; Utigard, T.; Taylor, M.P. Alumina agglomerates in aluminum smelters. In *Light Metals 1995*; Evans, J.W., Ed.; TMS: Warrendale, PA, USA, 1995; pp. 425–434.
5. Kuschel, G.I.; Welch, B.J. Further Studies of Alumina Dissolution under Conditions Similar to Cell Operation. In *Essential Readings in Light Metals: Volume 2 Aluminum Reduction Technology*; Bearne, G., Dupuis, M., Tarcy, G., Eds.; Springer: Cham, Switzerland, 2016; pp. 112–118. [[CrossRef](#)]
6. Kuschel, G.I.; Welch, B.J. Effect of Alumina Properties and Operation of Smelting Cells on the Dissolution Behavior of Alumina. In Proceedings of the Second International Alumina Quality Workshop, Perth, Australia, 14–19 October 1990; pp. 58–70.
7. Bagshaw, A.N.; Welch, B.J. The Influence of Alumina Properties on its Dissolution in Smelting Electrolyte. In *Essential Readings in Light Metals: Volume 1 Alumina and Bauxite*; Donaldson, D., Raahaage, B.E., Eds.; Springer: Cham, Switzerland, 2016; pp. 783–787. [[CrossRef](#)]
8. Yang, Y.; Gao, B.; Hu, X.; Wang, Z.; Shi, Z. Influence of LOI on Alumina Dissolution in Molten Aluminum Electrolyte. In *Molten Salts Chemistry and Technology*; John Wiley & Sons, Ltd.: Hoboken, NJ, USA, 2014; pp. 77–83. [[CrossRef](#)]
9. Lindsay, S.J. Key Physical Properties of Smelter Grade Alumina. In *Light Metals 2014*; Grandfield, J., Ed.; Wiley: Hoboken, NJ, USA, 2014; pp. 597–601. [[CrossRef](#)]
10. Alarie, J.; Kiss, L.I.; Dion, L.; Truchon, M.; Santerre, R.; Guérard, S.; Bilodeau, J.F. Empirical Prediction of Alumina Dissolution Rate in a Cryolitic Melt: Comparison with the Existing Literature. In *Light Metals 2022; The Minerals, Metals & Materials Series*; Eskin, D., Ed.; Springer: Cham, Switzerland, 2022; pp. 349–356. [[CrossRef](#)]
11. Alarie, J.; Kiss, L.I.; Poncsák, S.; Santerre, R.; Guérard, S.; Bilodeau, J.F. Influence of Additives on Alumina Dissolution in Superheated Cryolite Melts. In *Light Metals 2021; The Minerals, Metals & Materials Series*; Perander, L., Ed.; Springer: Cham, Switzerland, 2021; pp. 533–540. [[CrossRef](#)]
12. Isaeva, L.A.; Braslavskii, A.B.; Polyakov, P.V. Effect of the content of the α -phase and granulometric composition on the dissolution rate of alumina in cryolite-alumina melts. *Russ. J. Non-Ferr. Met.* **2009**, *50*, 600–605. [[CrossRef](#)]
13. Jain, R.K.; Tricklebank, S.; Welch, B.J.; Williams, D.J. Interaction of Aluminas with Aluminum Smelting Electrolytes. In *Light Metals 1983*; Adkins, E.M., Ed.; The Metallurgical Society of AIME: Wilkes-Barre, PA, USA, 1983; pp. 609–622.
14. Gerlach, J.; Hennig, U.; Kern, K. The dissolution of aluminum oxide in cryolite melts. *Metall. Mater. Trans.* **1975**, *6*, 83–86. [[CrossRef](#)]
15. Gylver, S.E.; Solheim, A.; Gudbrandsen, H.; Follo, Å.H.; Einarsrud, K.E. Lab Scale Experiments on Alumina Raft Formation. In *Light Metals 2020; The Minerals, Metals & Materials Series*; Tomsett, A., Ed.; Springer: Cham, Switzerland, 2020; pp. 659–663. [[CrossRef](#)]
16. Gylver, S.E.; Follo, Å.H.; Aulie, V.; Granlund, H.M.; Sørhuus, A.; Sandnes, E.; Einarsrud, K.E. On Gaseous Emissions During Alumina Feeding. In *Light Metals 2021; The Minerals, Metals & Materials Series*; Perander, L., Ed.; Springer: Cham, Switzerland, 2021; pp. 504–510. [[CrossRef](#)]
17. Kheiri, M.; Hennig, U.; Kammel, R. Krustenbildung und Krustenigenschaften beim Einsatz sekundärer Aluminiumoxide für die Aluminium-Reduktionselektrolyse. *Metall* **1989**, *43*, 858–862.
18. Kaszás, C. Behaviour of Alumina Powder Fed into Molten Electrolytic Bath. Ph.D. Thesis, Université du Québec à Chicoutimi, Chicoutimi, QC, Canada, 2020.
19. Yang, Y.; Gao, B.; Wang, Z.; Shi, Z.; Hu, X. Mechanism of Dissolution Behavior of the Secondary Alumina. *Metall. Mater. Trans. B Process. Metall. Mater. Process. Sci.* **2013**, *44*, 1296–1303. [[CrossRef](#)]

20. Bracamonte, L.; Einarsrud, K.E.; Rosenkilde, C.; Sandnes, E. Oxide Sensor Measurements and Simultaneous Optical Observations During Dissolution of Alumina in Cryolite Melt. In *Light Metals 2022; The Minerals, Metals & Materials Series*; Eskin, D., Ed.; Springer: Cham, Switzerland, 2022; pp. 381–391. [[CrossRef](#)]
21. Yang, Y.; Gao, B.; Wang, Z.; Shi, Z.; Hu, X.; Yu, J. Dispersion Caused by Carbon Dioxide During Secondary Alumina Dissolution: A Lab-Scale Research. *Metall. Mater. Trans. B* **2014**, *45*, 1150–1156. [[CrossRef](#)]
22. Kaszás, C.; Kiss, L.; Poncsák S.; Guérard, S.; Bilodeau, J.F. Spreading of Alumina and Raft Formation on the Surface of Cryolitic Bath. In *Light Metals 2017; The Minerals, Metals & Materials Series*; Ratvik, A.P., Ed.; Springer: Cham, Switzerland, 2017; pp. 473–478. [[CrossRef](#)]
23. Bracamonte, L. Development of an Electrochemical Sensor for Alumina Concentration Measurements and Dissolution Characteristics of Alumina in Cryolite Melt. Ph.D. Thesis, Norwegian University of Science and Technology, Trondheim, Norway, 2022.
24. Solheim, A.; Rolseth, S.; Skybakmoen, E.; Støen, L.; Sterten, Å.; Støre, T. Liquidus temperatures for primary crystallization of cryolite in molten salt systems of interest for aluminum electrolysis. *Metall. Mater. Trans. B* **1996**, *27*, 739–744. [[CrossRef](#)]
25. Skybakmoen, E.; Solheim, A.; Sterten, Å. Alumina solubility in molten salt systems of interest for aluminum electrolysis and related phase diagram data. *Metall. Mater. Trans. B* **1997**, *28*, 81–86. [[CrossRef](#)]
26. Schneider, C.A.; Rasband, W.S.; Eliceiri, K.W. NIH Image to ImageJ: 25 years of image analysis. *Nat. Methods* **2012**, *9*, 671–675. [[CrossRef](#)] [[PubMed](#)]